Available online at www.sciencedirect.com

SciVerse ScienceDirect

journal homepage: www.elsevier.com/locate/he

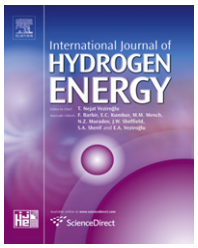

The effect of electrolyte type on performance of solid oxide fuel cells running on hydrocarbon fuels

*Meng Ni**

Building Energy Research Group, Department of Building and Real Estate, The Hong Kong Polytechnic University, Hung Hom, Kowloon, Hong Kong, China

ARTICLE INFO

Article history:
Received 19 October 2012
Received in revised form
23 November 2012
Accepted 9 December 2012
Available online 8 January 2013

Keywords:
Protonic ceramics
Solid oxide fuel cell
Hydrocarbon fuels
Electrochemical oxidation
Electrolyte
Internal reforming

ABSTRACT

A two-dimensional model is developed to simulate the performance of methane fueled solid oxide fuel cells (SOFCs), focusing on the effect of electrolyte type on SOFC performance. The model considers the heat and mass transfer, direct internal reforming (DIR) reaction, water gas shift reaction (WGSR), and electrochemical reactions in SOFCs. The electrochemical oxidation of CO in oxygen ion-conducting SOFC (O-SOFC) is considered. The present study reveals that the performance of H-SOFC is lower than that of O-SOFC at a high temperature or at a low operating potential, as electrochemical oxidation of CO in O-SOFC contributes to power generation. This finding is contrary to our common understanding that proton conducting SOFC (H-SOFC) always performs better than O-SOFC. However, at a high operating potential of 0.8 V or at a lower temperature, H-SOFC does exhibit better performance than O-SOFC due to its higher Nernst potential and higher ionic conductivity of the electrolyte. This indicates that the proton conductors can be good choices for SOFCs at intermediate temperature, even with hydrocarbons fuels. The results provide better understanding on how the electrolyte type influences the performance of SOFCs running on hydrocarbon fuels.

1. Introduction

Solid oxide fuel cells (SOFCs) are promising electrochemical energy conversion devices for clean power generation. One distinct feature of SOFCs is their fuel flexibility, as high operating temperature (i.e. 1073 K) enables internal reforming of hydrocarbon fuels or thermal cracking of ammonia in the porous anode of SOFC [1–3]. Thus, in principle all combustible fuels can be utilized in SOFCs for electricity generation, such as hydrogen, methane, methanol, ethanol, ammonia, dimethyl ether (DME) [4-7].

Conventionally SOFCs employ oxygen ion-conducting ceramics as electrolyte (here termed as O-SOFCs), such as yttria-stabilized zirconia (YSZ) [1]. In the recent years, proton conducting materials (i.e. $BaCeO_3$ doped with Gd or Sm) have also been demonstrated as good electrolyte materials for SOFCs (here termed as H-SOFCs) [8]. The use of proton conducting electrolyte in H-SOFC changes the location of steam production from the anode to the cathode, allowing high fuel utilization. In addition, due to a higher hydrogen concentration in the anode, the Nernst potential of H-SOFC is higher than that of O-SOFC. Several thermodynamic analyses have shown that the maximum efficiency of H-SOFC is higher than that of O-SOFC with H_2 and hydrocarbon fuels [9–12]. To examine the actual performance of H-SOFC considering various overpotential losses, electrochemical models have been developed to compare H-SOFC with O-SOFC [13–15]. The electrochemical modeling reveals that H-SOFC has lower

* Tel.: +852 2766 4152; fax: +852 2764 5131.
E-mail addresses: bsmengni@polyu.edu.hk, memni@graduate.hku.hk.
0360-3199/$ – see front matter
http://dx.doi.org/10.1016/j.ijhydene.2012.12.055

anode concentration overpotential than O-SOFC but the cathode overpotential in H-SOFC is considerably increased as the steam impedes the transport of oxygen [15]. Moreover, it's found that the actual performance of H-SOFC may not be higher than O-SOFC if the ionic conductivity of the electrolyte in H-SOFC is not higher than that of O-SOFC [13,15]. Recently, Ishak et al. [16] performed thermodynamic and an electrochemical modeling analyses, adopting the same methodologies with references [12,17] but a higher proton conductivity for H-SOFC. It's found that the H-SOFC performance is higher than O-SOFC, due to a lower ohmic overpotential of the electrolyte and higher hydrogen concentration in H-SOFC anode [16]. As the typical ionic conductivity of H-SOFC electrolyte is higher than that of YSZ for O-SOFC, it is expected that the actual performance of H-SOFC should be higher than that of O-SOFC.

In the above-mentioned studies on H-SOFC and O-SOFC, only H_2 is considered as an electrochemically active fuel and the electrochemical oxidation of CO is completely neglected. However, experimental investigations have confirmed the electrochemical oxidation of CO in the anode of O-SOFCs, although its reaction kinetics is lower than that of H_2 electrochemical oxidation [18–21]. Electrochemical oxidation of CO in O-SOFC can increase the current density and thus contribute to power generation. However, H-SOFC does not support CO electrochemical oxidation. Thus, O-SOFC should have an essential advantage over H-SOFC with hydrocarbon fuels. Our recent thermodynamic analysis shows when CO electrochemical oxidation is considered, the maximum efficiency of O-SOFC is higher than that of H-SOFC [22]. As the thermodynamic analysis does not consider any overpotential loss, it is still unknown which type of SOFC has higher actual performance. To answer this question, a two-dimensional model is developed to compare the actual performance of H-SOFC and O-SOFC considering CO electrochemical oxidation in O-SOFC anode. All the complicated physical–chemical processes are considered, including heat and mass transfer, direct internal reforming (DIR) reaction, water gas shift reaction (WGSR), and electrochemical reactions.

2. Model development

The working principles and computational domains for CH_4 fed H-SOFC and O-SOFC are shown in Fig. 1(a) and (b), respectively. The computational domain includes the interconnector, fuel channel, porous anode, dense electrolyte, porous cathode and the air channel. The anode-support configuration is adopted as it can yield higher SOFC performance than cathode-support and electrolyte-support configurations [13,15]. The planar configuration is used as it is widely used in practice. However, it is understood that the button cell configuration should be used for detailed comparison with experimental data, as experiments are usually conducted with button cells. In operation, pre-reformed methane gas mixture is supplied to the anode channel while air is supplied to the cathode channel. In both H-SOFC and O-SOFC, DIR of methane and WGSR take place in the porous anode, represented by Eqs. (1) and (2), respectively.

$$CH_4 + H_2O \leftrightarrow CO + 3H_2 \quad (1)$$

$$CO + H_2O \leftrightarrow CO_2 + H_2 \quad (2)$$

2.1. O-SOFC

In O-SOFC, oxygen molecules diffuse from the cathode surface to the cathode–electrolyte interface and react with electrons to produce oxygen ions (Eq. (3)), which are subsequently transported to the anode side via the dense oxygen ion-conducting electrolyte. At the anode side, H_2 and CO molecules transport to the triple-phase boundary (TPB) at the anode–electrolyte interface, where they react with oxygen ions to produce electrons, H_2O, and CO_2, as shown in Eqs. (4) and (5).

$$2e^- + 0.5O_2 \rightarrow O^{2-} \quad (3)$$

$$H_2 + O^{2-} \rightarrow H_2O + 2e^- \quad (4)$$

$$CO + O^{2-} \rightarrow CO_2 + 2e^- \quad (5)$$

The electrochemical oxidation of CH_4 is neglected due to its relatively low reaction kinetics [18]. In addition, reaction between CO_2 and CH_4 is not considered. Based on the working principles, a 2D thermo-electrochemical model is developed to simulate the coupled transport and reaction phenomena in O-SOFC. The 2D model consists of 3 sub-models: (1) an electrochemical model; (2) a chemical model; and (3) a computational fluid dynamics (CFD) model.

2.1.1. Electrochemical model

The electrochemical model is used to calculate the local current density (J) at given operating potentials (V). The use of interconnector with high electrical conductivity along the entire flow channel leads to uniform operating potential along the main flow stream. Thus, the J–V relationship can be established by solving the equations below [23].

$$V = E - \eta_{act,a} - \eta_{act,c} - \eta_{ohmic} \quad (6)$$

$$E_{H_2} = 1.253 - 0.00024516T + \frac{RT}{2F}\ln\left[\frac{P^I_{H_2}\left(P^I_{O_2}\right)^{0.5}}{P^I_{H_2O}}\right] \quad (7)$$

$$E_{CO} = 1.46713 - 0.0004527T + \frac{RT}{2F}\ln\left[\frac{P^I_{CO}\left(P^I_{O_2}\right)^{0.5}}{P^I_{CO_2}}\right] \quad (8)$$

where E is the equilibrium potential and the subscripts H_2 and CO represent the equilibrium potential associated with H_2 and CO fuels; T is temperature (K). R is the universal gas constant (8.3145 J mol^{-1} K^{-1}); and F is the Faraday constant (96,485 C mol^{-1}). P^I used in Eqs. (7) and (8) refers to the partial pressure at the electrode–electrolyte interface. Thus, the concentration overpotentials at the electrodes are included in the Nernst potential (E). η_{ohmic} is the ohmic overpotential and can be determined with the Ohm's law (Eq. (9)).

$$\eta_{ohmic} = JL\frac{1}{\sigma_{ionic}} \quad (9)$$

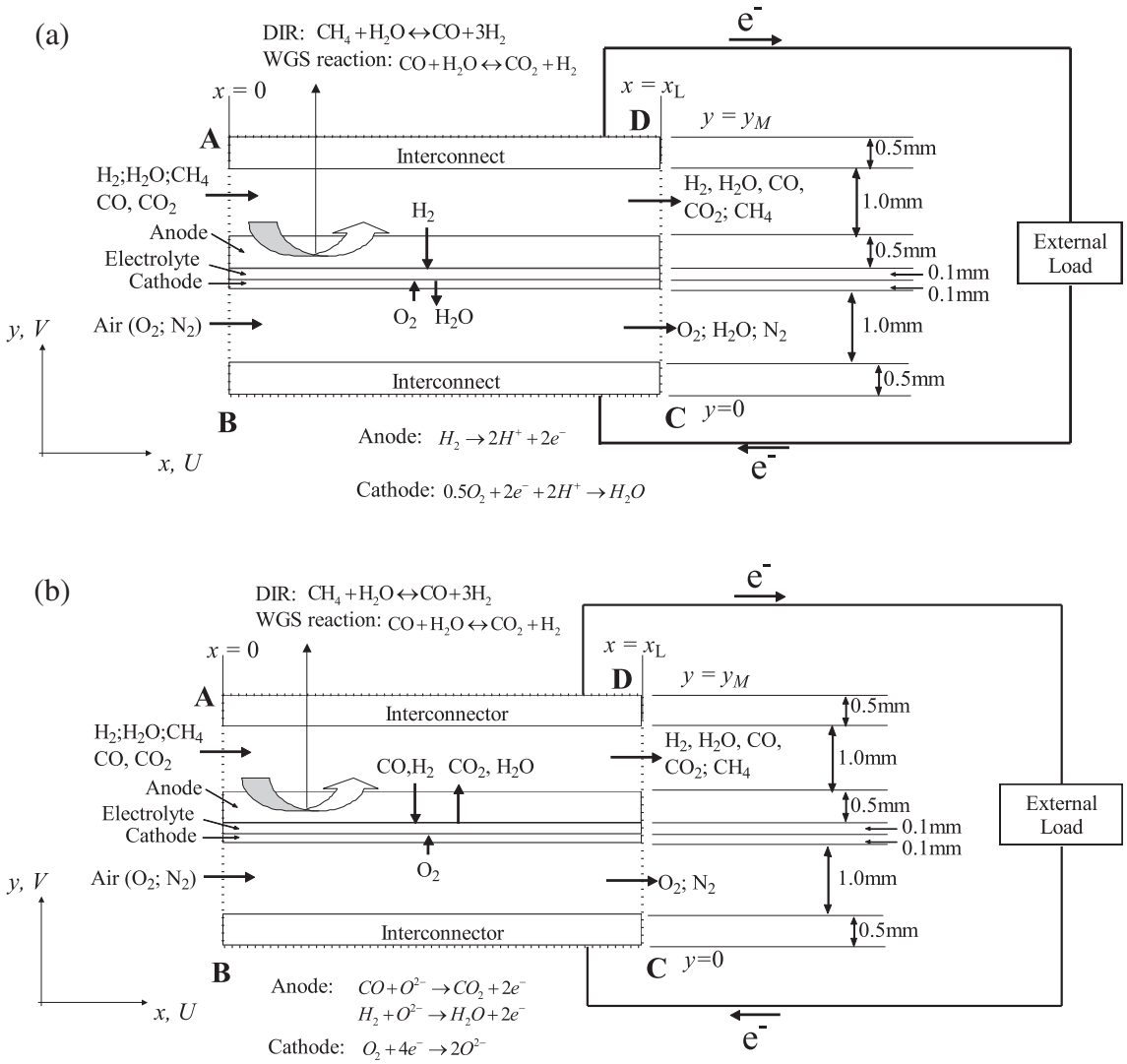

Fig. 1 – Working principles of methane-fed SOFCs (a) H-SOFC; (b) O-SOFC.

where L is the thickness (m) of the electrolyte and σ_{ionic} is the ionic conductivity (Ω^{-1} m^{-1}). J is the current density (A m^{-2}). According to Ferguson et al. [24], the ionic conductivity of YSZ electrolyte can be determined as,

$$\sigma_{ionic} = 3.34\times 10^4 \exp\left(-\frac{10,300}{T}\right) \quad (10)$$

$\eta_{act,a}$ and $\eta_{act,c}$ are activation overpotentials (V) at the anode and cathode, respectively. According to experiments, the activation overpotential and current density usually follow a linear relationship [25]. Thus, the activation overpotentials can be calculated as [26],

$$\eta_{act,H_2,i} = \frac{RTJ_{H_2}}{n_{H_2}FJ^0_{H_2,i}} \quad (11)$$

$$\eta_{act,CO,i} = \frac{RTJ_{CO}}{n_{CO}FJ^0_{CO,i}} \quad (12)$$

where $J^0_{H_2,i}$ and $J^0_{CO,i}$ are the exchange current densities (A m^{-2}) for electrochemical oxidation of H_2 and CO, respectively. The subscript i ($i = a$ and c) means the anode and cathode. J_{H_2} and J_{CO} are the current densities generated from H_2 fuel and CO fuel, respectively. According to the previous studies [26], the values of $J^0_{H_2,a}$ and $J^0_{H_2,c}$ at 1073 K are found to be 5300 A m^{-2} and 2000 A m^{-2} respectively. The electrochemical oxidation rate of H_2 is found to be 1.9–2.3 times and 2.3–3.1 times that of CO fuel at 1023 K and 1073 K, respectively [18]. Based on these experimental data, $J^0_{CO,a}$ is assumed to be $J^0_{CO,a} = 0.4J^0_{H_2,a}$. However, in the parametric simulations, $J^0_{CO,a} = 0.2J^0_{H_2,a}$ and $J^0_{CO,a} = 0.6J^0_{H_2,a}$ are also used.

The electrochemical model has been reported and validated in the previous publications for H_2 fuel and CH_4 fuel with internal reforming [13–15]. From the parametric simulations, it is known that the ohmic overpotential and the activation overpotential are the major source of potential losses [13,14]. The concentration overpotential loss is usually very low, although it may limit the SOFC performance at very high current density [13,15,26].

2.1.2. *Chemical model*

The chemical model is used to calculate the reaction rates of DIR and WGSR and the corresponding reaction heat. According to Haberman and Young [27], the reaction rates for DIR

(R_{DIR}, mol m^{-3} s^{-1}) and WGSR (R_{WGSR}, mol m^{-3} s^{-1}) can be calculated below.

$$R_{DIR} = k_{rf}\left(P_{CH_4}P_{H_2O} - \frac{P_{CO}\left(P_{H_2}\right)^3}{K_{pr}}\right) \tag{13}$$

$$k_{rf} = 2395\exp\left(\frac{-231,266}{RT}\right) \tag{14}$$

$$R_{WGSR} = k_{sf}\left(p_{H_2O}p_{CO} - \frac{p_{H_2}p_{CO_2}}{K_{ps}}\right) \tag{15}$$

$$k_{sf} = 0.0171\exp\left(\frac{-103,191}{RT}\right) \quad (\text{mol m}^{-3}\,\text{Pa}^{-2}\,\text{s}^{-1}) \tag{16}$$

$$K_{ps} = \exp(-0.2935Z^3 + 0.6351Z^2 + 4.1788Z + 0.3169) \tag{17}$$

$$Z = \left(\frac{1000}{T(K)}\right) - 1 \tag{18}$$

$$K_{pr} = 1.0267\times10^{10}\times\exp(-0.2513Z^4 + 0.3665Z^3 + 0.5810Z^2 - 27.134Z + 3.277) \tag{19}$$

The reaction heat associated with DIR reaction and WGSR can be determined from the enthalpy changes of the two reactions. The heat generation from exothermic WGSR (H_{WGSR}, J mol^{-1}) and heat consumption by endothermic DIR reaction (H_{DIR}, J mol^{-1}) can be approximated as [23].

$$H_{DIR} = -(206,205.5 + 19.5175T) \tag{20}$$

$$H_{WGSR} = 45,063 - 10.28T \tag{21}$$

2.1.3. *Computational fluid dynamic (CFD) model*

The CFD model is developed to simulate the heat and mass transfer in SOFCs. The relatively low gas velocity and small dimension of SOFC result in low Reynolds number. Therefore, the gas flow in SOFC is typically laminar. From heat transfer analysis, it is found that the temperature difference between the solid and the gas in the porous electrodes is negligibly small [28]. Thus local thermal equilibrium condition is adopted. The governing equations for the CFD model include mass conservation, momentum conservation, energy conservation, and species conservation [23,29].

$$\frac{\partial(\rho U)}{\partial x} + \frac{\partial(\rho V)}{\partial y} = S_m \tag{22}$$

$$\frac{\partial(\rho UU)}{\partial x} + \frac{\partial(\rho VU)}{\partial y} = -\frac{\partial P}{\partial x} + \frac{\partial}{\partial x}\left(\mu\frac{\partial U}{\partial x}\right) + \frac{\partial}{\partial y}\left(\mu\frac{\partial U}{\partial y}\right) + S_x \tag{23}$$

$$\frac{\partial(\rho UV)}{\partial x} + \frac{\partial(\rho VV)}{\partial y} = -\frac{\partial P}{\partial y} + \frac{\partial}{\partial x}\left(\mu\frac{\partial V}{\partial x}\right) + \frac{\partial}{\partial y}\left(\mu\frac{\partial V}{\partial y}\right) + S_y \tag{24}$$

$$\frac{\partial(\rho c_P UT)}{\partial x} + \frac{\partial(\rho c_P VT)}{\partial y} = \frac{\partial}{\partial x}\left(k\frac{\partial T}{\partial x}\right) + \frac{\partial}{\partial y}\left(k\frac{\partial T}{\partial y}\right) + S_T \tag{25}$$

$$\frac{\partial(\rho UY_i)}{\partial x} + \frac{\partial(\rho VY_i)}{\partial y} = \frac{\partial}{\partial x}\left(\rho D_{i,m}^{eff}\frac{\partial Y_i}{\partial x}\right) + \frac{\partial}{\partial y}\left(\rho D_{i,m}^{eff}\frac{\partial Y_i}{\partial y}\right) + S_{sp} \tag{26}$$

U and V are the velocity components in x and y directions; ρ and μ are the gas density and viscosity of the gas mixture respectively, which depends on local temperature and gas composition.

$$\rho = \frac{1}{\sum_{i=1}^{N} Y_i/\rho_i} \tag{27}$$

where ρ_i and Y_i are the density and mass fraction of gas species i.

The viscosity of the gas mixture (μ) can be calculated as [30]

$$\mu = \sum_{i=1}^{n}\frac{y_i\mu_i}{\sum_{j=1}^{n} y_j\varphi_{ij}} \tag{28}$$

where the value of φ_{ij} can be obtained by Herning and Zipperer approximation as [30]

$$\varphi_{ij} = \sqrt{\frac{M_j}{M_i}} = \varphi_{ji}^{-1} \tag{29}$$

where M_i is molecular weight of species i (kg kmol^{-1}).

In the porous catalyst layer, effective heat conductivity (k) and heat capacity (c_p) are used and can be calculated as [31]

$$k = \varepsilon k_f + (1-\varepsilon)k_s \tag{30}$$

$$c_p = \varepsilon c_{p,f} + (1-\varepsilon)c_{p,s} \tag{31}$$

The effective diffusion coefficients $D_{i,m}^{eff}$ can be determined as,

$$\frac{1}{D_{i,m}^{eff}} = \begin{cases} \dfrac{\xi}{\varepsilon}\left(\dfrac{\sum_{j\neq i}\frac{X_j}{D_{ij}}}{1-X_i} + \dfrac{3}{2r_p}\sqrt{\dfrac{\pi M_i}{8RT}}\right), & \text{in porous electrodes} \\ \dfrac{\sum_{j\neq i}\frac{X_j}{D_{ij}}}{1-X_i}, & \text{in gas channels} \end{cases} \tag{32}$$

$$D_{ij} = \frac{0.0026T^{1.5}}{p\sqrt{\dfrac{2M_iM_j}{M_j+M_i}}\left(\dfrac{\sigma_i+\sigma_j}{2}\right)^2\Omega_D} \tag{33}$$

$$\Omega_D = \frac{1.06036}{\left(\frac{k_bT}{\varepsilon_{i,j}}\right)^{0.1561}} + \frac{0.193}{\exp\left(0.47635\left(\frac{k_bT}{\varepsilon_{i,j}}\right)\right)} + \frac{1.03587}{\exp\left(1.52996\left(\frac{k_bT}{\varepsilon_{i,j}}\right)\right)} + \frac{1.76474}{3.89411\left(\frac{k_bT}{\varepsilon_{i,j}}\right)} \tag{34}$$

where ξ and ε are the tortuosity and porosity of electrodes; and r_p is the average radius of pores. D_{ij} is the binary diffusion coefficient of species i and j. σ is the mean characteristic length of species and Ω_D is a dimensionless diffusion collision. k_b is the Boltzmann's constant (1.38066×10^{-23} J K^{-1}). The values of σ_i and $\varepsilon_{i,j}$ used in the present study are summarized in Table 1 [30]. X_i is the molar fraction of specie i. The relationship between mass fraction (Y_i) and molar fraction can be determined as.

$$Y_i = X_i\left(\frac{M_i}{\sum_{i=1}^{N} X_iM_i}\right) \tag{35}$$

The Darcy's law is used as source terms in the momentum equation (Eqs. (23) and (24)).

Table 1 – Values of σ_i and ε_i/k for calculating the diffusion coefficients [30].

	CO	CO_2	H_2	O_2	CH_4	N_2	H_2O
σ_i (Å)	3.69	3.941	2.827	3.467	3.758	3.798	2.641
ε_i/k ($K^2\ J^{-1}$)	91.7	195.2	59.7	106.7	148.6	71.4	809.1

$$S_x = -\frac{\mu U}{B_g} \tag{36}$$

$$S_y = -\frac{\mu V}{B_g} \tag{37}$$

where B_g is the permeability (m^2). Typical value of permeability (i.e. $2 \times 10^{-10}\ m^2$) is used for the SOFC electrodes while infinitely large value (i.e. $10^{20}\ m^2$) is used for the gas channels, so that the momentum equations can be applied to both the gas channels and the porous electrodes.

The source term (S_T, W m^{-3}) in the energy equation (Eq. (25)) accounts for heat associated with DIR reaction and WGSR, heat from electrochemical reactions, and heat from irreversible overpotential losses. In the present simulation, the source term in the porous anode comes from the reaction heat for DIR reaction and WGSR. The heat from electrochemical reaction and irreversible overpotential losses are evenly applied to the dense electrolyte. Thus, the source term S_T can be written as [23],

$$S_T = \begin{cases} R_{DIR}H_{DIR} + R_{WGSR}H_{WGSR}, & \text{in porous anode} \\ -\dfrac{J_{H_2}T\Delta S_{H_2} + J_{CO}T\Delta S_{CO}}{2FL} + \dfrac{J_{H_2}\eta_{t,H_2}}{L} + \dfrac{J_{CO}\eta_{t,CO}}{L}, & \text{in electrolyte} \end{cases} \tag{38}$$

where ΔS_{H_2} and ΔS_{CO} are the entropy changes for electrochemical reactions associated with H_2 fuel and CO fuel, respectively. η_{t,H_2} and $\eta_{t,CO}$ are the total overpotential losses for H_2 fuel and CO fuel.

The source term (S_{sp}, kg m^{-3} s^{-1}) in the species equation (Eq. (26)) represent species consumption or generation due to the chemical and electrochemical reactions. Taking H_2 as an example, the source term (S_{H_2}) in the species equation can be written as [23,32],

$$S_{H_2} = \begin{cases} 3R_{DIR}M_{H_2} + R_{WGSR}M_{H_2}, & \text{in porous anode} \\ -\dfrac{J_{H_2}M_{H_2}}{2F\Delta y}, & \text{at the anode–electrolyte interface} \end{cases} \tag{39}$$

where Δy is the control volume width in y-direction (Fig. 1) at the anode–electrolyte interface.

2.2. H-SOFC

In H-SOFC, both DIR reaction and WGSR also occur in the porous anode. However, only H_2 can participate in the electrochemical reaction and contribute to power generation. The 3 sub-models for O-SOFC in the previous section can be adapted to H-SOFC. Since CO is not electrochemically active in H-SOFC, only Eq. (7) is solved for calculating the Nernst potential of H-SOFC. As steam is electrochemically produced in the porous cathode, the partial pressure of H_2O in the cathode should be used in Eq. (7) for H-SOFC. The exchange current densities used for O-SOFC are adopted for H-SOFC for calculating the activation overpotential losses. According to Matsumoto [33], the proton conductivity of the $BaCe_{0.8}Y_{0.2}O_{3-\alpha}$ electrolyte is about 2.6 S m^{-1} at 973 K and 3.5 S m^{-1} at 1073 K. Assuming linear dependence on temperature for simplicity, the proton conductivity (σ_{ionic}, S m^{-1}) at different temperatures can be determined as,

$$\sigma_{ionic} = 0.009T - 6.157 \tag{40}$$

3. Numerical methodologies

A constant velocity is specified at the inlet ($x = 0$) of gas flow channel and zero velocity is applied to the solid part and the porous layers. At the bottom and top of the computational domain ($y = 0$ and $y = y_M$), thermally adiabatic conditions are adopted. At the outlet of the computational domain ($x = x_L$), zero gradients for temperature, velocity, and mass fraction are assumed for the gas channels while zero velocity is applied to the solid part and the porous layer.

The governing equations are discretized and solved with the finite volume method (FVM). The diffusion terms and the convection terms are treated with the central difference and upwind schemes, respectively. The pressure and velocity are linked with the SIMPLEC algorithm. The discretized equations are solved with the TDMA based iteration schemes. The program starts with initialization by assuming initial data over the whole computational domain. Then, the chemical model is solved to calculate the reaction rates of DIR and WGSR as well as the corresponding reaction heat. After that, the electrochemical model is solved to determine the local current density at a given operating potential. The results obtained from the chemical model and electrochemical model are used to determine the source terms in the CFD model. After solving the CFD model, the flow field, temperature field, gas distributions, etc can be updated. If not converged, the updated data will be used to solve the chemical model again. Computation is repeated until convergence is achieved. The program is written in FORTRAN and has been well validated by comparing the simulation results with data from the literature as well as from FLUENT.

4. Results and analysis

In this section, simulations are performed to compare the actual performance of O-SOFC and H-SOFC, with consideration of CO electrochemical oxidation in O-SOFC. The typical simulation conditions are summarized in Table 2 [23,34]. It is understood that many parameters affect the SOFC performance, such as the cell size, the cell configuration, the catalyst used etc. For example, longer cells will have larger gas composition variation along the channel and high concentration loss in the downstream. In button cells, the gas flowing into the cell is opposite to the gas flowing out from the cell, thus the gas flow, heat transfer and the cell performance could be different from the planar cells [35–38]. However, this

paper does not aim to study all parameters but focuses on the comparison between H-SOFC and O-SOFC with hydrocarbon fuels. The important parameters that affect the CO electrochemical oxidation are studied in detail, such as the exchange current density for CO fuel, temperature and operating potential.

4.1. *Comparison between H-SOFC and O-SOFC*

Simulations are performed at an inlet temperature of 973 K and an inlet gas velocity (anode) of 0.5 m s^{-1} to compare the current density distributions in H-SOFC and O-SOFC. $J^0_{CO} = 0.6J^0_{H_2}$ and $J^0_{CO} = 0.2J^0_{H_2}$ are used for simulating the performance of O-SOFC. The quantitative contribution from CO electrochemical oxidation to the O-SOFC performance can be seen from the current density by CO fuel (Fig. 2). As can be seen from Fig. 2(a), the current densities of O-SOFC are higher than that of H-SOFC, due to significant contribution of CO electrochemical oxidation for power generation in O-SOFC (Fig. 2(b)). In addition, the current density of O-SOFC increases considerably as the reaction rate of CO electrochemical oxidation is increased (from $J^0_{CO} = 0.2J^0_{H_2}$ to $J^0_{CO} = 0.6J^0_{H_2}$). This result is contrary to our common understanding that H-SOFC always perform better than O-SOFC due to higher Nernst potential of H-SOFC and higher ionic conductivity of the proton conducting electrolyte [10,11,16]. However, according to the author's best knowledge, no experimental comparison of H-SOFC and O-SOFC with hydrocarbon fuels has been reported in the literature. Once experimental data are available, the model developed in the present paper can be better validated and improved for design optimization.

Table 2 – Parameters used in simulation [23,34].

Parameter	Value
Operating temperature, T (K)	973
Operating pressure, P (bar)	1.0
Electrode porosity, ε	0.4
Electrode tortuosity, ξ	3.0
Average pore radius, r_p (μm)	0.5
Anode-supported electrolyte	
Anode thickness, d_a (μm)	500
Electrolyte thickness, L (μm)	100
Cathode thickness, d_c (μm)	100
Height of gas flow channel (mm)	1.0
Length of the planar SOFC (mm)	20
Thickness of interconnector (mm)	0.5
Inlet velocity at anode: U_0 (m s^{-1})	0.5
Cathode inlet gas molar ratio: O_2/N_2	0.21/0.79
Anode inlet gas molar ratio: $H_2O/CH_4/H_2/CO_2/CO$	0.003/0.116/0.661/0.002/0.218 [34]
SOFC operating potential (V)	0.4
Thermal conductivity of SOFC component (W m^{-1} K^{-1})	
Anode	11.0
Electrolyte[a]	2.7
Cathode	6.0
Interconnect	1.1

a Thermal conductivity of proton conductor is assumed to be the same with oxygen ion conductor.

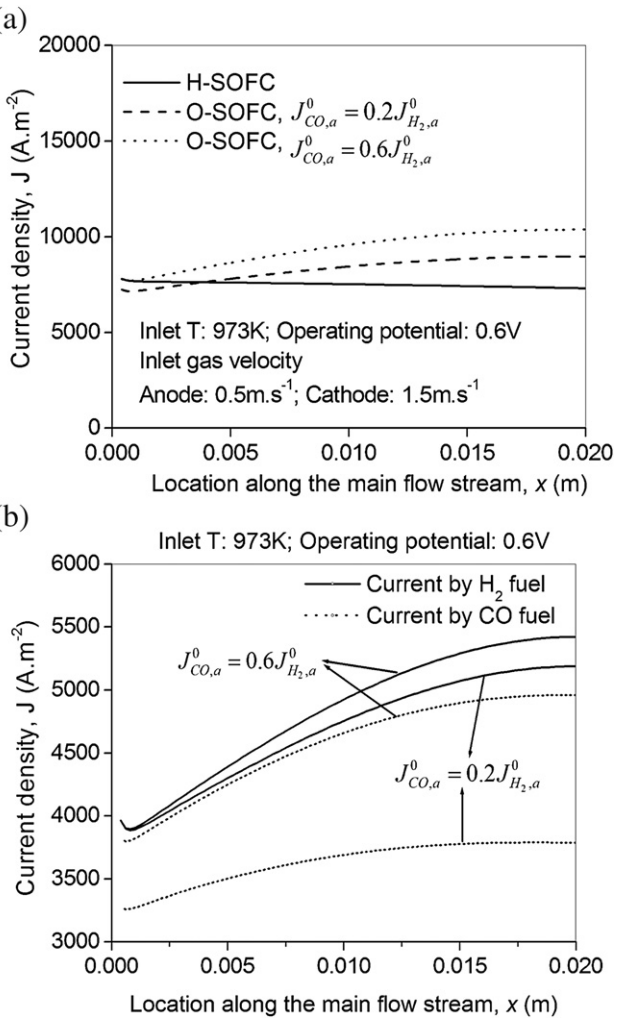

Fig. 2 – Distributions of current density in SOFCs at an inlet temperature of 973 K and operating potential of 0.6 V – (a) comparison between H-SOFC and O-SOFC; (b) current density generated by CO fuel and H_2 fuel in O-SOFC.

The distributions of DIR reaction rate in H-SOFC and O-SOFC at an operating potential of 0.6 V are investigated and compared in Fig. 3. Using the model by Haberman and Young [27], the DIR reaction rates are in general very low (less than 1 mol m^{-3} s^{-1}) at an inlet temperature of 973 K. The DIR in H-SOFC is slightly negative and decreases along the flow channel (Fig. 3(a)). In H-SOFC, H_2O from electrochemical reaction is produced in the cathode, which tends to reverse the DIR reaction in anode. For comparison, the DIR in O-SOFC is positive and increases along the cell (Fig. 3(b) and (c)), as H_2O from electrochemical reaction is produced in the anode and favors positive DIR reaction. When the CO electrochemical oxidation is increased (from $J^0_{CO} = 0.2J^0_{H_2}$ to $J^0_{CO} = 0.6J^0_{H_2}$), the DIR reaction rate is slightly increased. The increase in DIR

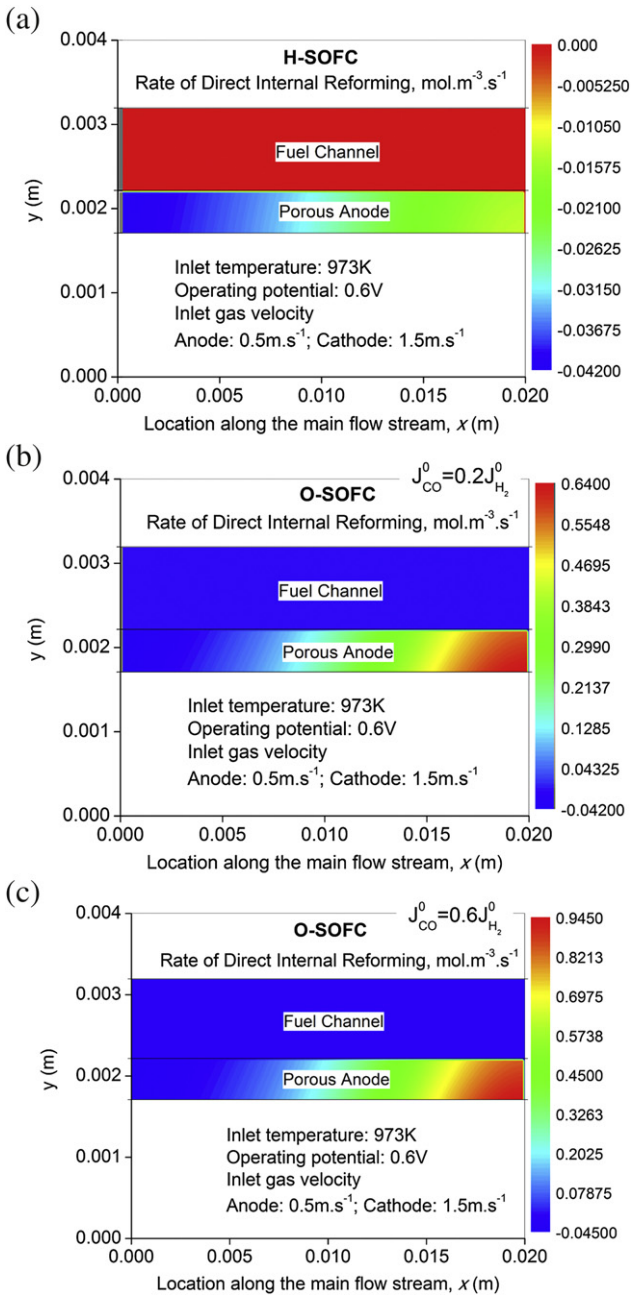

Fig. 3 – Distributions of DIR reaction rate in SOFCs at an inlet temperature of 973 K and operating potential of 0.6 V – (a) H-SOFC; (b) O-SOFC with $J^0_{CO}=0.2J^0_{H_2}$; and (c) O-SOFC with $J^0_{CO}=0.6J^0_{H_2}$.

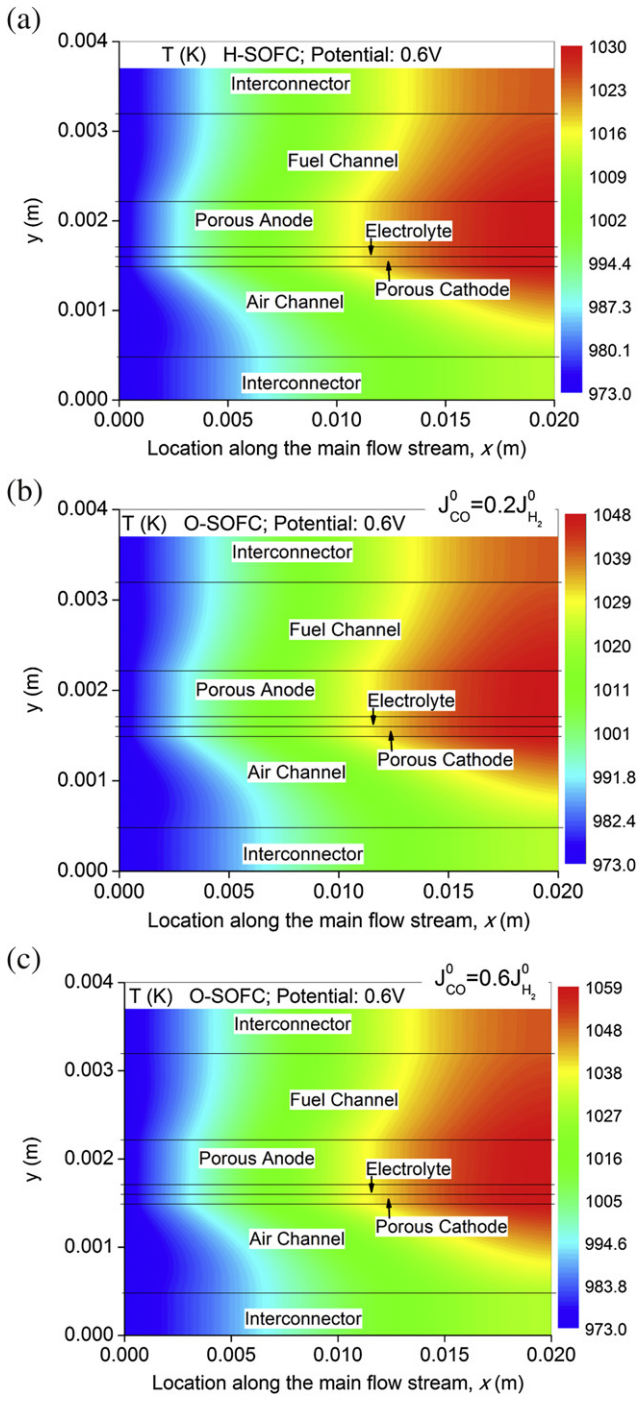

Fig. 4 – Distributions of temperature in SOFCs at an inlet temperature of 973 K and operating potential of 0.6 V – (a) H-SOFC; (b) O-SOFC with $J^0_{CO}=0.2J^0_{H_2}$; and (c) O-SOFC with $J^0_{CO}=0.6J^0_{H_2}$.

reaction rates in O-SOFC is caused by increased cell temperature in the downstream (Fig. 4). The temperature in SOFCs depends on 3 factors: (1) entropy change of the electrochemical reactions; (2) irreversible overpotential losses; and (3) chemical reactions including DIR reaction and WGSR. Both (1) and (2) contribute to heat generation and are related to current density. For chemical reactions, positive DIR reaction is endothermic and consumes heat while positive WGSR is exothermic and generates heat. For both H-SOFC and O-SOFC, the increase of temperature along the main flow stream indicates that the total heat generation greatly exceeds the heat consumption by chemical reactions. The temperature in O-SOFC is higher than that of H-SOFC as the higher current density in O-SOFC generates more heat from (1) and (2). For example, at $J^0_{CO}=0.6J^0_{H_2}$, the SOFC temperature is increased from 973 K at the inlet to be about 1059 K at the outlet (Fig. 4(c)).

The distribution of WGSR rate in H-SOFC shows quite different pattern from that in O-SOFC (Fig. 5(a)–(c)). In H-SOFC, reaction rate of WGSR is negative and increases along the cell (Fig. 5(a)), due to relatively lower H_2O molar fraction in the anode. For comparison, reaction rate of WGSR in O-SOFC is positive and increases along the cell at $J^0_{CO} = 0.2J^0_{H_2}$ (Fig. 5(b)). At $J^0_{CO} = 0.6J^0_{H_2}$, the WGSR reaction rate is positive and high at the middle of the cell and small at the two ends (Fig. 5(c)). This phenomenon can be explained by a lower CO molar fraction in O-SOFC at $J^0_{CO} = 0.6J^0_{H_2}$ than the other two cases (Fig. 6(a)–(c)), which tends to reverse the WGSR in the downstream. As can be seen from Fig. 6(b) and (c), the CO molar fraction in O-SOFC is obviously lower than that in H-SOFC, especially at $J^0_{CO} = 0.6J^0_{H_2}$, since CO is electrochemically oxidized in O-SOFC. Due to positive DIR and WGSR reaction rates in O-SOFC while negative DIR and WGSR reaction rates in H-SOFC, O-SOFC shows higher H_2 molar fraction than that of H-SOFC in the downstream (Fig. 7(a)–(c)).

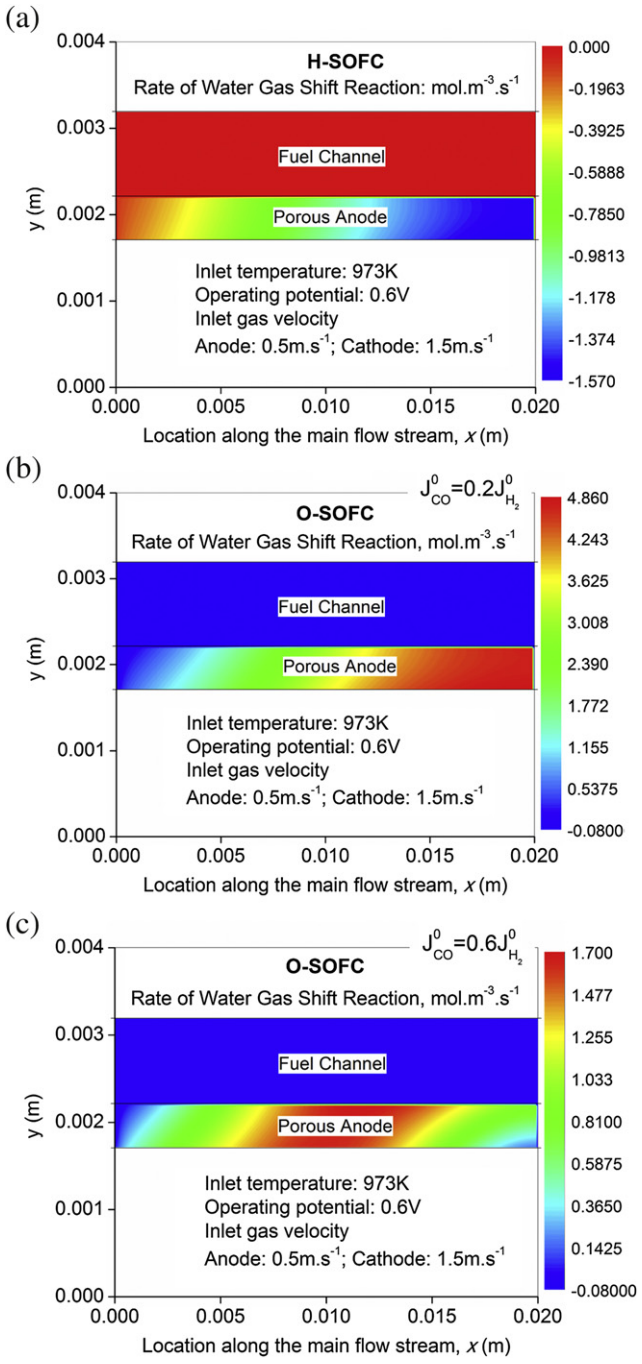

Fig. 5 – Reaction rates of WGSR in SOFCs at an inlet temperature of 973 K and operating potential of 0.6 V – (a) H-SOFC; (b) O-SOFC with $J^0_{CO} = 0.2J^0_{H_2}$; and (c) O-SOFC with $J^0_{CO} = 0.6J^0_{H_2}$.

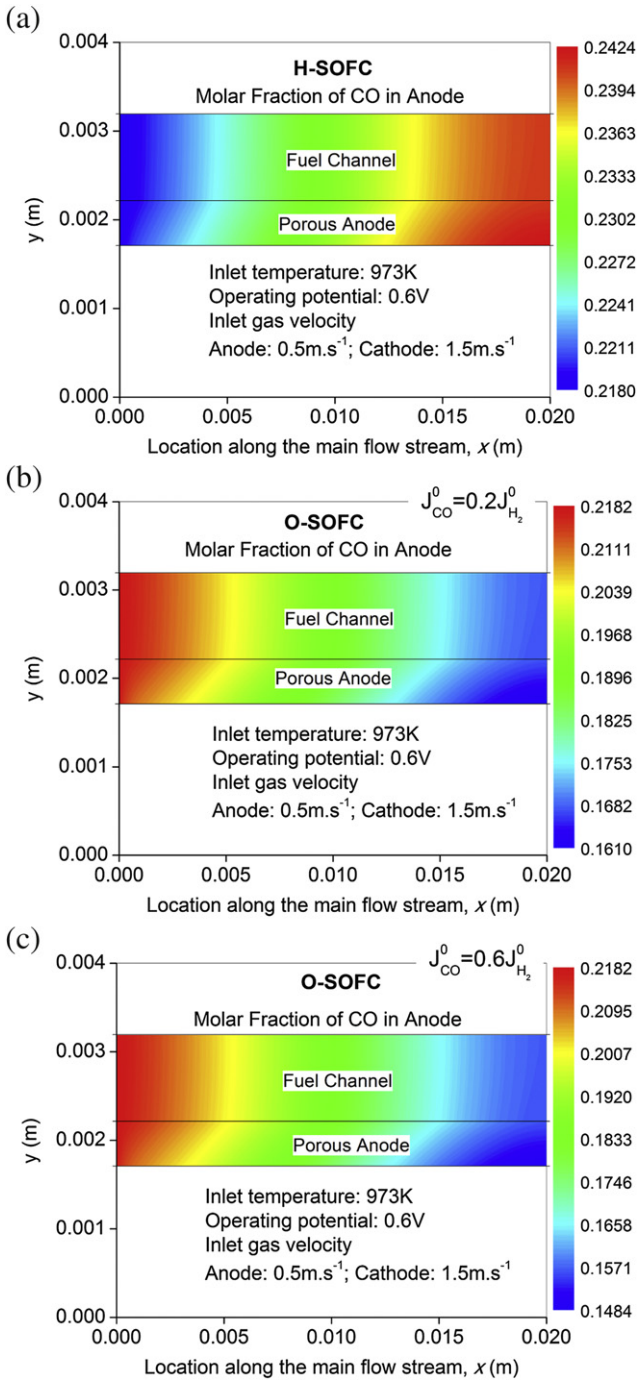

Fig. 6 – Molar fractions of CO in SOFCs at an inlet temperature of 973 K and operating potential of 0.6 V – (a) H-SOFC; (b) O-SOFC with $J^0_{CO} = 0.2J^0_{H_2}$; and (c) O-SOFC with $J^0_{CO} = 0.6J^0_{H_2}$.

It should be mentioned that in SOFC performance characterization, fuel utilization is also a usually used parameter. At a given operating temperature and cell configuration, the fuel utilization is directly linked with the current density. In other words, high current density corresponds to high fuel utilization and low current density corresponds to low fuel utilization [39]. Therefore, the current density is sufficient to quantify the SOFC performance and thus the detailed analyses on the fuel utilization are not provided in this paper.

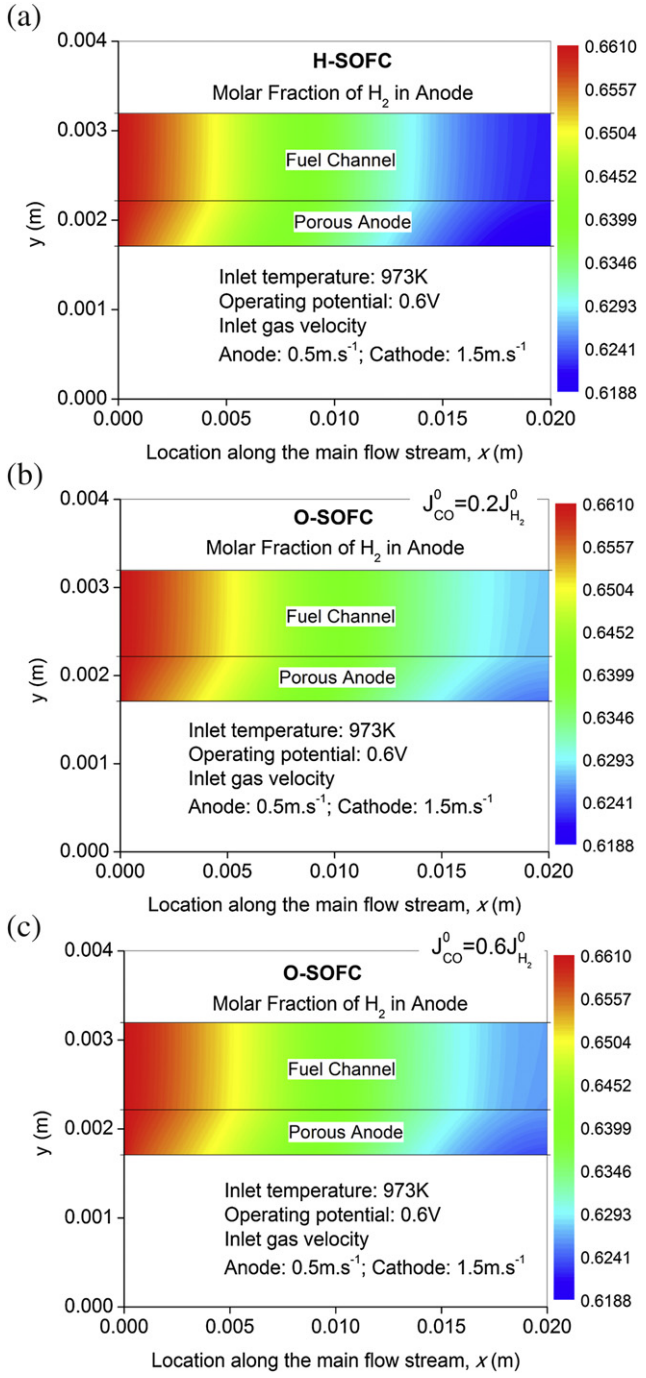

Fig. 7 – Molar fractions of H_2 in SOFCs at an inlet temperature of 973 K and operating potential of 0.6 V – (a) H-SOFC; (b) O-SOFC with $J^0_{CO}=0.2J^0_{H_2}$; and (c) O-SOFC with $J^0_{CO}=0.6J^0_{H_2}$.

4.2. *Effect of operating potential*

The effect of operating potential is studied by increasing the operating potential from 0.6 V to 0.8 V. At 0.8 V, the H-SOFC shows higher average current density than O-SOFC (Fig. 8). This is due to a high Nernst potential of H-SOFC [10,12] and small contribution from CO fuel in O-SOFC at a high potential. The distributions of temperature, DIR reaction rate, WGSR reaction rate and CO molar fraction are shown in Fig. 9. At 0.8 V, the temperature increases along the main flow stream in both H-SOFC and O-SOFC (Fig. 9(a) and (b)), but the increments are smaller than at an operating potential of 0.6 V (Fig. 4(a) and (b)). This is because the current density is lower at a higher operating potential, which in turn generates less heat from reversible entropy change and irreversible overpotential losses. In addition, the distributions of DIR reaction rates, WGSR reaction rates and gas composition at 0.8 V exhibit smaller variations along the gas flow channel (Fig. 9(c)–(h)) than at 0.6 V, due to smaller current density and lower average temperature at 0.8 V than at 0.6 V.

4.3. *Effect of operating temperature*

To examine the effect of temperature on SOFC performance, simulations are performed at inlet temperatures of 873 K and 1073 and at $J^0_{CO}=0.4J^0_{H_2}$ for O-SOFC. Results are shown in Fig. 10. Interestingly, it is found that the performance of H-SOFC is higher than that of O-SOFC at an inlet temperature of 873 K (Fig. 10(a)). This is because the ionic conductivity of proton conductors is considerably higher than that of oxygen ion conductors [24,33] and the contribution from CO electrochemical oxidation in O-SOFC is too small at a low temperature (Fig. 10(c)). However, at a higher inlet temperature (1073 K), O-SOFC performs significantly better than H-SOFC (Fig. 10(b)), due to significant contribution of CO electrochemical reaction to power generation (Fig. 10(c)). These results indicate that O-SOFC should be used at high temperatures while H-SOFC can be a good choice at intermediate temperatures, even with hydrocarbon fuels. Since there is

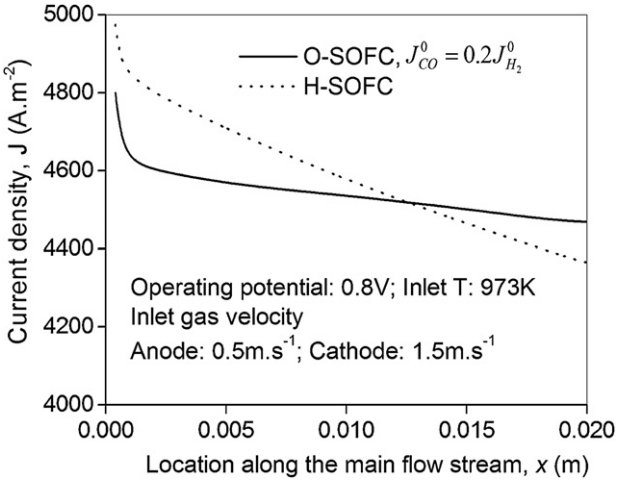

Fig. 8 – Current density comparison between H-SOFC and O-SOFC at an operating potential of 0.8 V.

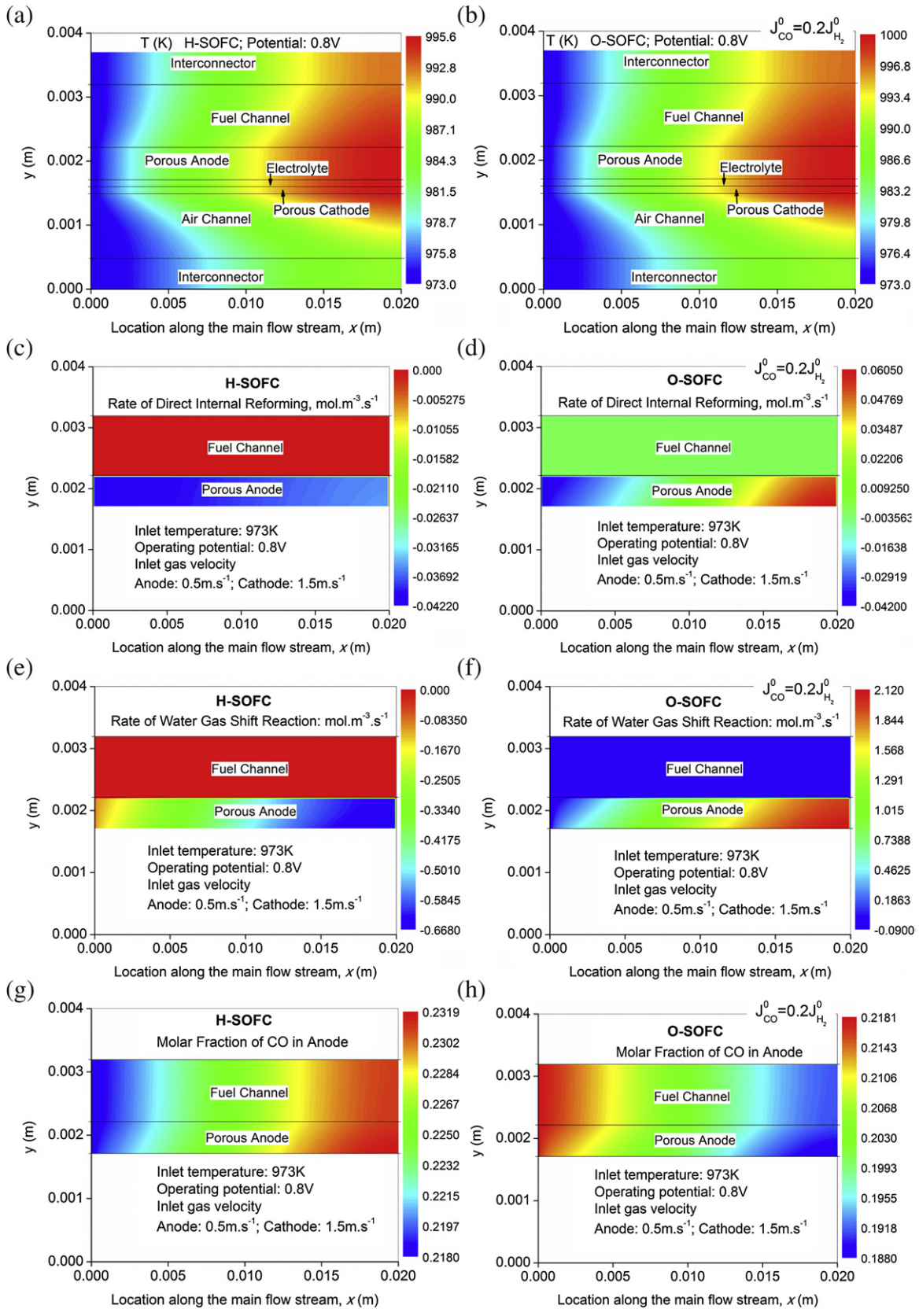

Fig. 9 – Comparison between H-SOFC and O-SOFC (with $J^0_{CO}=0.2J^0_{H_2}$) at an inlet temperature of 973 K and operating potential of 0.8 V – (a) temperature in H-SOFC; (b) temperature in O-SOFC; (c) reaction rate of DIR in H-SOFC; (d) reaction rate of DIR in O-SOFC; (e) reaction rate of WGSR in H-SOFC; (f) reaction rate of WGSR in O-SOFC; (g) molar fraction of CO in H-SOFC; and (h) molar fraction of CO in O-SOFC.

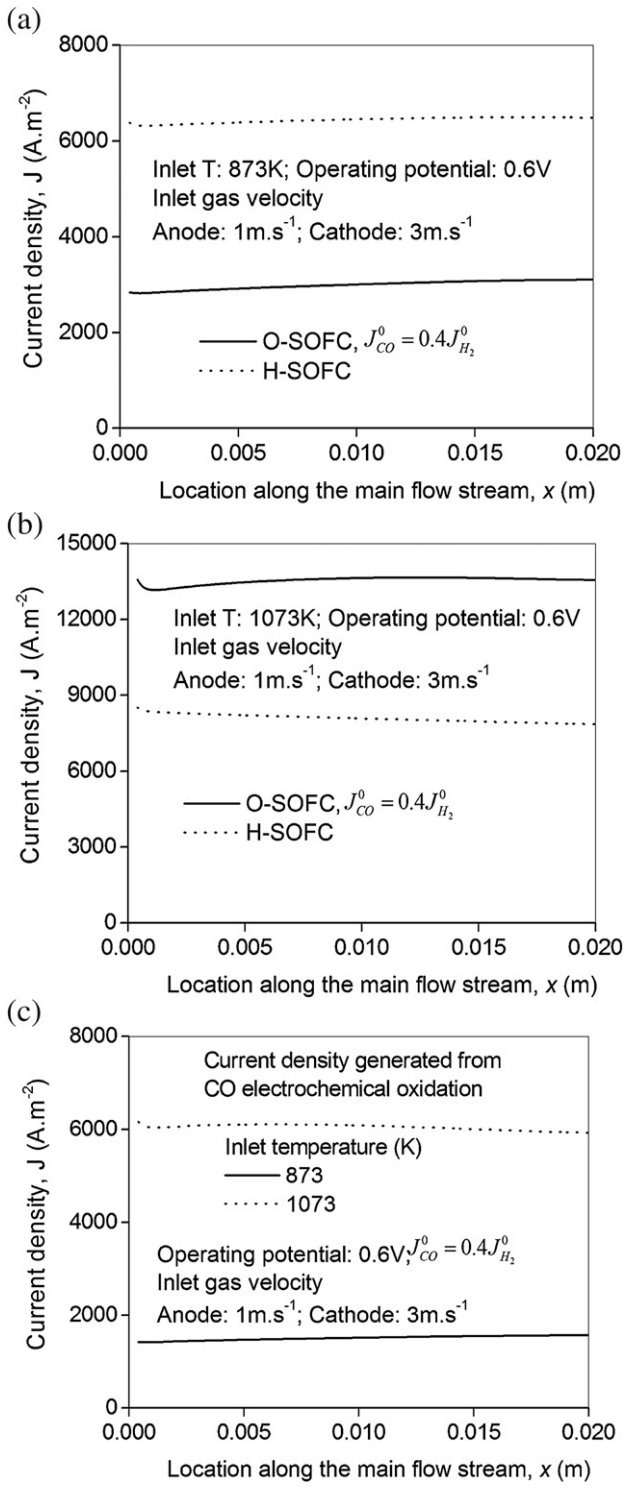

Fig. 10 – Current density comparison between H-SOFC and O-SOFC at an operating potential of 0.6 V – (a) inlet temperature of 873 K; (b) inlet temperature of 1073 K; (c) current density generated by CO fuel in O-SOFC.

a trend to lowering the operating temperature of SOFCs [40], proton conductors should be given more consideration for the development of high performance intermediate temperature SOFCs.

5. Conclusions

A two-dimensional mathematical model is developed to study the performance of methane-fed SOFCs, with a focus on the comparison between H-SOFC and O-SOFC. The model consists of an electrochemical model, a chemical model and a CFD model. Electrochemical oxidation of CO in the anode of O-SOFC is considered.

Contrary to our common understanding that H-SOFC always performs better than O-SOFC, the present study shows that the performance of H-SOFC is evidently lower than that of O-SOFC at an operating potential of 0.6 V and at 973 K, as CO electrochemical oxidation in O-SOFC contributes to power generation. The difference between H-SOFC and O-SOFC is enlarged when the CO electrochemical oxidation is enhanced ($J^0_{CO} = 0.6J^0_{H_2}$). The WGSR and DIR in H-SOFC are both negative at 973 V and 0.6 V, due to a relatively lower molar fraction of H_2O in the anode. For comparison, the DIR and WGSR in O-SOFC are both positive. The temperatures in both H-SOFC and O-SOFC are found to increase along the cell, due to large heat generation by electrochemical reaction and overpotential losses. However, it's also found that H-SOFC exhibits higher performance at a high operating potential than O-SOFC due to small contribution by CO fuel in O-SOFC. In addition, H-SOFC is found to perform better than O-SOFC at an intermediate temperature (873 K), due to its higher ionic conductivity of the electrolyte.

The results presented in the paper reveal that H-SOFC exhibits advantages with H_2 fuel (or ammonia). With hydrocarbon fuels, O-SOFC performs better than H-SOFC at typical operating temperatures (i.e. 1073 K) due to the contribution from CO fuel. However, at a reduced temperature (i.e. 873 K), H-SOFC exhibits higher performance and thus the proton conductors can be good choices for SOFCs at intermediate temperatures. The results provide better understanding on how the electrolyte type influences the SOFC performance.

Acknowledgments

This research was supported by a grant (Project Number: PolyU 5238/11E) from Research Grant Council (RGC) of Hong Kong.

Nomenclature

B_g	permeability of the porous electrode, m^2
c_p	heat capacity, J kg^{-1} K^{-1}
d_a	thickness of anode, μm
d_c	thickness of cathode, μm
$D^{eff}_{i,m}$	effective diffusion coefficient of species i in gas mixture, cm^2 s^{-1}
$D_{i,k}$	Knudsen diffusion coefficient of i, cm^2 s^{-1}
$D_{i,j}$	binary diffusion coefficient of i and j, cm^2 s^{-1}
E	equilibrium potential, V
E_0	reversible potential at standard condition, V
F	Faraday constant, 9.6485×10^4 C mol^{-1}

H_{DIR}	heat demand for direct internal reforming of methane, J mol^{-1}
H_{WGS}	heat generation from water gas shift reaction, J mol^{-1}
J	current density, A m^{-2}
k	thermal conductivity, W m^{-1} K^{-1}
L	thickness of the electrolyte, m
M_i	molecular weight of species i, kg mol^{-1}
n	number of electrons transferred
P	operating pressure, bar
P_i^I	partial pressure, bar, of species i at electrode–electrolyte interface
R_{DIR}	reaction rate of direct internal reforming of methane, mol m^{-3} s^{-1}
R_{WGSR}	rate of water gas shift reaction, mol m^{-3} s^{-1}
r_p	mean pore radius of electrode, μm
R	universal gas constant, 8.3145 J mol^{-1} K^{-1}
ΔS	entropy change of electrochemical reactions, kJ kg^{-1} K^{-1}
S_m	source term in continuity equation, kg m^{-3} s^{-1}
S_x, S_y	source terms in momentum equations, kg m^{-2} s^{-2}
S_T	source terms in energy equations, W m^{-3}
S_{sp}	source terms in species equations, kg m^{-3} s^{-1}
T	operating temperature, K
U	velocity in x direction, m s^{-1}
U_{in}	gas velocity at the SOFC inlet, m s^{-1}
V	SOFC operating potential, V; velocity in y direction, m s^{-1}
X	molar fraction of species i
Y	mass fraction of species i
ε	electrode porosity
ξ	electrode tortuosity
$\sigma_{i,j}$	mean characteristic length of species i and j, Å
σ_{ionic}	ionic conductivity of the electrolyte, Ω^{-1} m^{-1}
Ω_D	dimensionless diffusion collision integral
ρ	density of the gas mixture, kg m^{-3}
μ	viscosity of gas mixture, kg m^{-1} s^{-1}
$\eta_{act,a}$	activation overpotential at anode, V
$\eta_{act,c}$	activation overpotential at cathode, V
η_{ohmic}	ohmic overpotential of the electrolyte, V

REFERENCES

[1] Singhal SC, Kendall K. High temperature solid oxide fuel cells – fundamentals, design and applications. New York: Elsevier; 2003.

[2] Colpan CO, Dincer I, Hamdullahpur F. Thermodynamic modeling of direct internal reforming solid oxide fuel cells operating with syngas. Int J Hydrogen Energy 2007;32:787–95.

[3] Shiratori Y, Ijichi T, Oshima T, Sasaki K. Internal reforming SOFC running on biogas. Int J Hydrogen Energy 2010;35:7905–12.

[4] Achenbach E, Riensche E. Methane/steam reforming kinetics for solid oxide fuel cells. J Power Sources 1994;52:283–8.

[5] Su C, Ran R, Wang W, Shao ZP. Coke formation and performance of an intermediate-temperature solid oxide fuel cell operating on dimethyl ether fuel. J Power Sources 2011; 196:1967–74.

[6] Liu MF, Peng RR, Dong DH, Gao JF, Liu XQ, Meng GY. Direct liquid methanol-fueled solid oxide fuel cell. J Power Sources 2008;185:188–92.

[7] Ma QL, Peng RR, Lin YJ, Gao JF, Meng GY. A high-performance ammonia-fueled solid oxide fuel cell. J Power Sources 2006; 161:95–8.

[8] Peng RR, Wu Y, Yang LZ, Mao ZQ. Electrochemical properties of intermediate-temperature SOFCs based on proton conducting Sm-doped $BaCeO_3$ electrolyte thin film. Solid State Ionics 2006;177:389–93.

[9] Demin A, Tsiakaras P. Thermodynamic analysis of a hydrogen fed solid oxide fuel cell based on a proton conductor. Int J Hydrogen Energy 2001;26:1103–8.

[10] Demin AK, Tsiakaras PE, Sobyanin VA, Hramova SY. Thermodynamic analysis of a methane fed SOFC system based on a protonic conductor. Solid State Ionics 2002;152-153:555–60.

[11] Jamsak W, Assabumrungrat S, Douglas PL, Laosiripojana N, Charojrochkul S. Theoretical performance analysis of ethanol-fueled solid oxide fuel cells with different electrolytes. Chem Eng J 2006;119:11–8.

[12] Ni M, Leung DYC, Leung MKH. Thermodynamic analysis of ammonia fed solid oxide fuel cells: comparison between proton-conducting electrolyte and oxygen ion conducting electrolyte. J Power Sources 2008;183:682–6.

[13] Ni M, Leung MKH, Leung DYC. Mathematical modeling of proton-conducting solid oxide fuel cells and comparison with oxygen ion conducting counterpart. Fuel Cells 2007;7: 269–78.

[14] Ni M, Leung DYC, Leung MKH. Modeling of methane fed solid oxide fuel cells: comparison between proton conducting electrolyte and oxygen ion conducting electrolyte. J Power Sources 2008;183:133–42.

[15] Ni M, Leung DYC, Leung MKH. Mathematical modeling of ammonia-fed solid oxide fuel cells with different electrolytes. Int J Hydrogen Energy 2008;33:5765–72.

[16] Ishak F, Dincer I, Zamfirescu C. Thermodynamic analysis of ammonia-fed solid oxide fuel cells. J Power Sources 2012;202: 157–65.

[17] Ni M, Leung DYC, Leung MKH. An improved electrochemical model for the NH_3 fed proton conducting solid oxide fuel cells at intermediate temperatures. J Power Sources 2008;185: 233–40.

[18] Matsuzaki Y, Yasuda I. Electrochemical oxidation of H_2 and CO in a H_2–H_2O–CO–CO_2 system at the interface of a Ni–YSZ cermet electrode and YSZ electrolyte. J Electrochemical Soc 2000;147:1630–5.

[19] Yurkiv V, Starukhin D, Volpp HR, Bessler WG. Elementary reaction kinetics of the CO/CO_2/Ni/YSZ electrode. J Electrochemical Soc 2011;158:B5–10.

[20] Habibzadeh B, Becker BP, Sukeshini AM, Jackson GS. CO electrochemical oxidation on Ni patterned anodes for assessing SOFC kinetics. ECS Trans 2008;11:53–61.

[21] Sukeshini AM, Habibzadeh B, Becker BP, Stoltz CA, Eichhorn BW, Jackson GS. Electrochemical oxidation of H_2, CO, and CO/H_2 mixtures on patterned Ni anodes on YSZ electrolytes. J Electrochemical Soc 2006;153:A705–15.

[22] Sun Q, Zheng KQ, Ni M. Thermodynamic analysis of methane-fueled SOFCs considering CO electrochemical oxidation, submitted for publication.

[23] Ni M. Modeling of SOFC running on partially pre-reformed gas mixture. Int J Hydrogen Energy 2012;37:1731–45.

[24] Ferguson JR, Fiard JM, Herbin R. Three-dimensional numerical simulation for various geometries of solid oxide fuel cells. J Power Sources 1996;58:109–22.

[25] Personal communication with Dr. M. S. Sohal from Idaho National Laboratory, at ASME 2010 8th international fuel cell science, engineering & technology conference, June 14–16, 2010, Brooklyn, New York, USA.

[26] Chan SH, Khor KA, Xia ZT. A complete polarization model of a solid oxide fuel cell and its sensitivity to the change of cell component thickness. J Power Sources 2001;93:130–40.

[27] Haberman BA, Young JB. Three-dimensional simulation of chemically reacting gas flows in the porous support structure of an integrated-planar solid oxide fuel cell. Int J Heat Mass Transfer 2004;47:3617–29.
[28] Zheng KQ, Sun Q, Ni M. On the local thermal non-equilibrium in SOFCs considering internal reforming and ammonia thermal cracking reaction. Energ Technol, in press.
[29] Wang CY. Fundamental models for fuel cell engineering. Chem Rev 2004;104:4727–65.
[30] Reid RC, Prausnitz JM, Poling BE. The properties of gases & liquids. 4th ed. New York: McGraw-Hill Book Company; 1987.
[31] Yuan JL, Lv XR, Sunden B, Yue DT. Analysis of parameter effects on transport phenomena in conjunction with chemical reactions in ducts relevant for methane reformers. Int J Hydrogen Energy 2007;32:3887–98.
[32] Ni M. On the source terms of species equations in fuel cell modeling. Int J Hydrogen Energy 2009;34:9543–4.
[33] Matsumoto H. Proton-conducting perovskite – properties and experiences for hydrogen transport and energy applications. In: Prospects protonic ceramic cells 2011 – international workshop on protonic ceramic fuel cell and steam electrolysis: status and prospects, 3–4 November 2011, Botanical Institute, Montpellier, France.
[34] Zhu HY, Kee RJ. Two-dimensional model of distributed charge transfer and internal reforming within unit cells of segmented-in-series solid-oxide fuel cells. J Power Sources 2011;196:7654–64.
[35] Zinovik I, Poulikakos D. Modeling the temperature field in the reforming anode of a button-shaped solid oxide fuel cell. Electrochim Acta 2009;54:6234–43.
[36] Goldin GM, Zhu HY, Kee RJ, Bierschenk D, Barnett SA. Multidimensional flow, thermal, and chemical behavior in solid oxide fuel cell button cells. J Power Sources 2009;187:123–35.
[37] Xie YY, Xue XJ. Multi-scale electrochemical reaction anode model for solid oxide fuel cells. J Power Sources 2012;209:81–9.
[38] Shi YX, Cai NS, Li C. Numerical modeling of an anode-supported SOFC button cell considering anodic surface diffusion. J Power Sources 2007;164:639–48.
[39] Ni M. Thermo-electrochemical modeling of ammonia-fueled solid oxide fuel cells considering ammonia thermal decomposition in the anode. Int J Hydrogen Energy 2011;36:3153–66.
[40] Wachsman ED, Lee KT. Lowering the temperature of solid oxide fuel cells. Science 2011;334:935–9.